**Section 1.** Derivation and significance of the critical equilibrium contact angle θ_c for transition between the Wenzel and Cassie-Baxter states.

There are numerous notational schemes and conventions used in the literature for describing the various parameters that correlate the changes in apparent contact angle with the texture of a wetting or non-wetting substrate. Care must be taken in defining these parameters, especially for re-entrant textures considered in the present work.
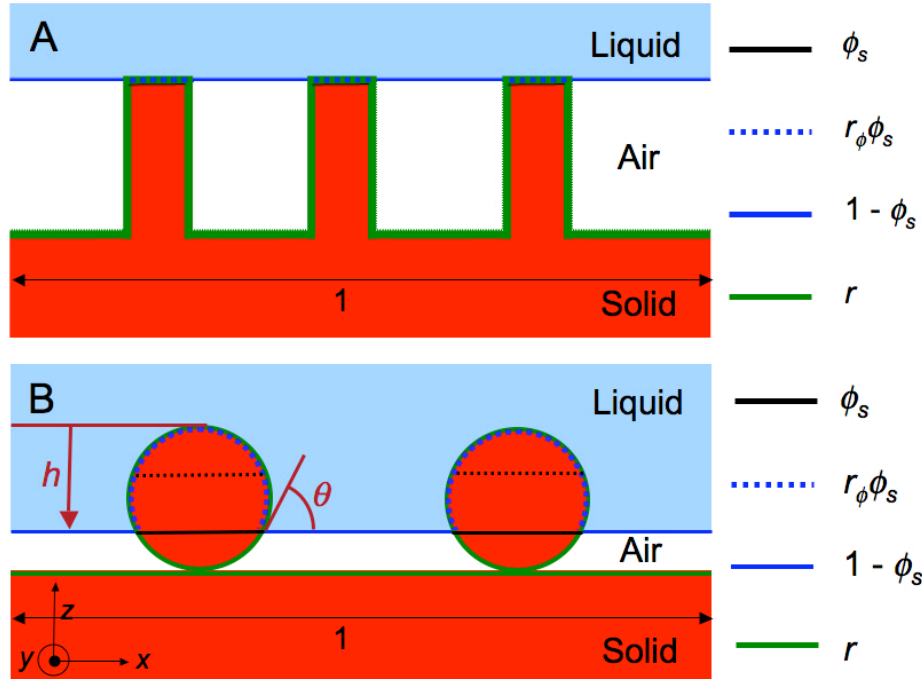
Figure S1. A schematic illustrating the various characteristic geometrical parameters used in the *Wenzel* and *Cassie-Baxter* relations for two different substrates (a) A flat-topped array of vertical pillars and (b) an array of cylinders possessing re-entrant texture. We assume that the gap between the features is significantly less than the capillary length for the liquid, an assumption that holds true for the various textures considered in this work. Thus, the liquid-vapor interface may be considered approximately flat, as shown in the figure.

The apparent contact angle (θ^*) for a fully wetted interface is typically described using the Wenzel relation (1), which can be written as:

$$\cos\theta^* = r\cos\theta \qquad\qquad\qquad \text{(s1-1)}$$

where the surface roughness r is defined as the total surface area divided by the projected surface area and θ is the equilibrium contact angle defined as the contact angle on a

smooth surface possessing identical surface chemistry as the textured surface. By definition $r \geq 1$. On the other hand, the apparent contact angle on a composite interface is given by the Cassie-Baxter relation (2), which can be written as:

$$\cos\theta^* = f_1 \cos\theta + f_2(-1) = f_1 \cos\theta - f_2 \qquad (s1\text{-}2)$$

Here f_1 is the total area of the solid-liquid interface divided by the projected area and f_2 is the total area of the liquid-vapor interface divided by the projected area. In his recent work, Marmur (3) noted that it is convenient to write $f_1 = r_\phi\phi_s$ and $f_2 = 1-\phi_s$, where ϕ_s is the area fraction of the liquid-air interface occluded by the texture (shown as ▬ in Fig. S1) and r_ϕ is the 'roughness' of the wetted area, that is the actual wetted area compared to the occluded area. For surface textures such as the one shown in Fig. S1b, it is important to recognize that both r_ϕ and ϕ_s are complicated functions of the surface topography and the equilibrium contact angle θ. By definition $\phi_s \leq 1$ and $r_\phi \geq 1$. Therefore, the product $f_1 = r_\phi\phi_s$ may be greater or less than 1. It should also be noted that even though ϕ_s is a function of the penetration depth h (Fig. S1b), a re-entrant geometry can have the same value of ϕ_s at different values of h, as shown in Fig. S1b, where the occluded area denoted by ▬ is the same as the occluded area denoted by ┈┈ . As the penetration depth h for the surface shown in Fig. S1b is directly related to the equilibrium contact angle (to enable $\theta = \psi$, as discussed in detail in the main manuscript), this implies that two different contacting liquids, with greatly differing surface tensions, can yield similar values for the variable ϕ_s. However, it is clear from Fig. S1b that the product $f_1 = r_\phi\phi_s$ is always uniquely defined for a given value of h or θ. Thus, Eq. s1-2 may be re-written as:

$$\cos\theta^* = r_\phi\phi_s \cos\theta + \phi_s - 1 \qquad (s1\text{-}3)$$

This extended form of the Cassie-Baxter relation may be referred to as a generalized textural wetting equation. It is clear that Eq. s1-3 reduces to the Wenzel relation (Eq. s1-1) in the limit of a fully wetted interface, when $\phi_s \to 1$ and $r_\phi\phi_s \to r$ (also see Fig. S1b). It should be noted that the form of the Cassie-Baxter relation provided in Eq. s1-3 is somewhat different from the simplified form of the relation widely used in the literature (4, 5), given as:

$$\cos\theta^* = \phi_s \cos\theta + \phi_s - 1 \qquad (s1\text{-}4)$$

2

A comparison of Eq. s1-3 and s1-4 shows that Eq. s1-4 is only valid in the limiting case of $r_\phi = 1$, which is accurate only for textured surfaces such as a flat-topped pillar surface (for example those shown in Fig. S1a). This is one of the most commonly considered surfaces in the literature as vertical arrays of flat-topped pillars can be readily created by photo-lithography (4, 6-10). However, it is clear that the roughness of the wetted area r_ϕ can be significantly greater than unity for textures such as the re-entrant geometries considered in the present work or the pillar arrays with nano-textured tops considered by McCarthy et al. (11).

The critical value of the equilibrium contact angle (θ_c) beyond which the composite interface leads to a lower overall free energy in comparison to the fully-wetted interface can be determined by equating the Wenzel (Eq. s1-1) and Cassie-Baxter (Eq. s1-3) relations as:

$$\cos\theta_c = \frac{-(1-\phi_s)}{(r-r_\phi\phi_s)} \tag{s1-5}$$

From Fig. S1b it is clear that the fraction of the projected area of the solid surface that is wet by the liquid (ϕ_s) is always less than unity. Also, the total area of the solid-liquid interface divided by the projected area ($r_\phi\phi_s$), must be smaller than or equal to the total surface area divided by the projected area (r). Indeed $r_\phi\phi_s$ monotonically increases to approach r in the limit of the fully-wetted interface. This understanding implies that the right hand side of Eq. s1-5 is always negative or that $\theta_c > 90°$.

Section 2. Computing the variation in Gibbs free energy for the propagation of a liquid on a textured surface.
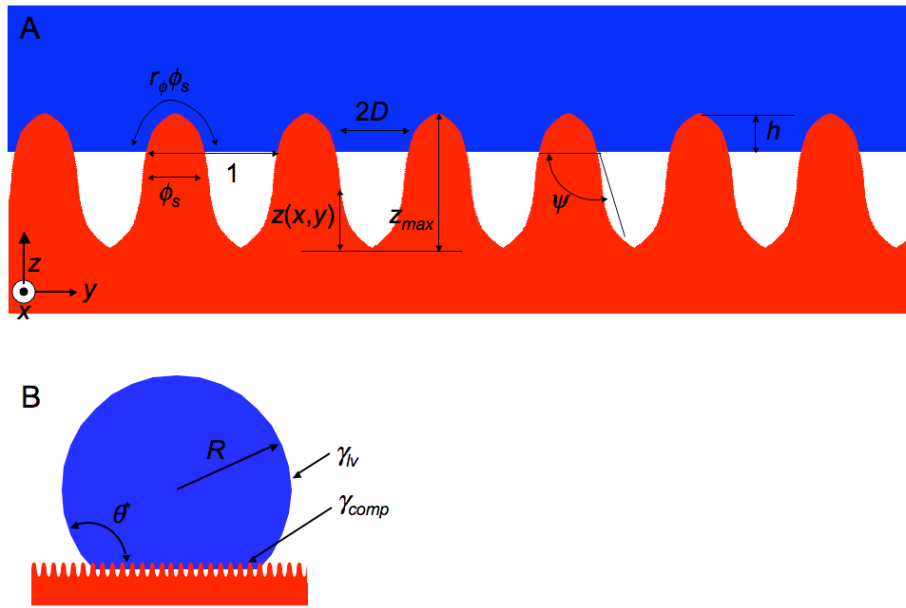
Figure S2. A schematic illustrating the various parameters used in the calculation of the change in the Gibbs free energy density on the propagation of the liquid-air interface.

As a liquid propagates into the texture of a solid substrate, the original liquid-air and solid-air interfaces are progressively replaced by the liquid-solid interface, leading to a loss or gain in the overall free energy of the system. The liquid will spontaneously wick into the texture, leading to a fully-wetted interface, if the liquid surface can continuously lower its overall free energy as it penetrates in to the solid texture. On the other hand, a composite interface (with the liquid sitting partially on air) can also lead to a stable thermodynamic state, if the overall free energy for the system attains a local or global minimum, before the liquid reaches the bottom of the surface texture. Marmur (3) used this idea to predict the stability of a composite interface (eq. 9 of reference (3)) on any rough surface. We build on Marmur's work and calculate the actual change in the Gibbs free energy density (G^* = (*free energy of the system*) / (*original surface area of drop*)) associated with the propagation of the solid-liquid interface on a textured substrate, from the reference point of a liquid drop. The results from these calculations can be used to predict both the feasibility of attaining a composite interface on a particular surface, as well as the apparent contact angles associated with each local or global equilibrium state.

For our calculations, for any given distance h of the liquid – air interface from the top of the textured substrate (normalized with respect to the maximum height of the surface z_{max}; see Fig. S2a), we first assume a number of different values for the temporary apparent contact angle θ_t^* such that $0° < \theta_t^* < 180°$. Next, we compute the areal Gibbs free energy density (G^*) of the liquid drop for a given θ_t^* and h/z_{max}, with respect to a reference state of $G^* = 0$ at $h/z_{max} = 0$, as (3):

$$G^* = \gamma_{lv}\pi R^2(-2 - 2\cos\theta_t^* - \sin^2\theta_t^*(r_\phi\phi_s\cos\theta_t^* + \phi_s - 1)) \Big/ 4\pi R_0^2 \qquad \text{(s2-1)}$$

and $R = R_0\left(4\Big/(2 - 3\cos\theta_t^* + \cos^3\theta_t^*)\right)^{1/3}$

where R = radius of the drop in contact with the surface at an angle θ_t^*, R_0 = original radius of drop (at $h/z_{max} = 0$), r_ϕ is the roughness of the wetted area and ϕ_s is the area fraction of the liquid-air interface occluded by the solid texture, as shown in Fig. S2a. It should be noted that both r_ϕ and ϕ_s are functions of h. Also, the θ_t^* value which minimizes the areal Gibbs free energy density will be equal to the apparent contact angle θ^* computed using the Cassie-Baxter relation (2) (the Cassie-Baxter relation collapses to the Wenzel relation (1) in the limit of the fully-wetted interface).

To numerically compute G^*, we developed a *Matlab®* (Mathworks Inc.) code with the following steps:

1. Given the data for a surface profile $(z = z(x,y))$, for any value of h/z_{max}, find the wetted region by comparing z and h/z_{max} and thus compute ϕ_s.

2. Integrate to find the total wetted area, and hence compute r_ϕ.

3. Calculate G^* as a function of θ_t^*, ϕ_s and r_ϕ. A minimum in G^* corresponds to a point of local equilibrium. We also compute the magnitude of the energy barrier around each equilibrium point.

Based on these ideas, we have computed the areal Gibbs free energy density variation for water ($\gamma_{lv} = 72.1$ mN/m, $\theta = 120°$) and hexadecane ($\gamma_{lv} = 27.5$ mN/m, $\theta = 80°$) propagating on three different surfaces:

1. A surface composed of vertical pillars with $r = 1.8$ and $\phi_s = 0.4$ (Fig. S3).

2. A model electrospun surface with average fiber radius $R = 0.5$ μm, average inter-fiber spacing $2D = 2.7$ μm. This leads to $r = 1.8$; $r_\phi \phi_s$ (water) $= 0.28$, ϕ_s (water) $= 0.23$; $r_\phi \phi_s$ (hexadecane) $= 0.44$ and ϕ_s (hexadecane) $= 0.27$ (Fig. S4).

3. A micro-hoodoo surface with the hoodoo width $W = 10$ μm, inter-hoodoo spacing $2D = 10$ μm and the hoodoo height $H = 7$ μm. This leads to ($r = 2.0$; $r_\phi \phi_s$ (water) $= 0.45$, ϕ_s (water) $= 0.44$; $r_\phi \phi_s$ (hexadecane) $= 0.46$ and ϕ_s (hexadecane) $= 0.44$ (Fig. S5).
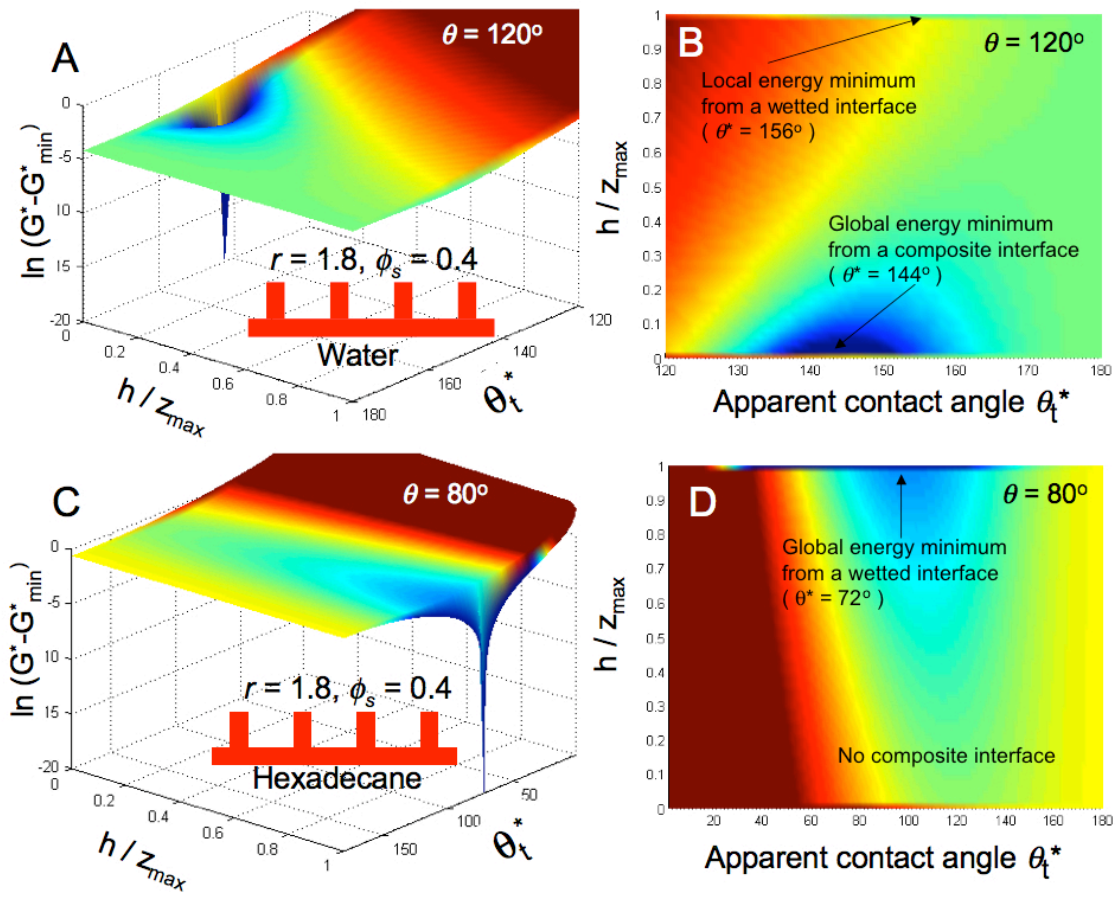
Figure S3a. The change in the areal Gibbs free energy density, as a function of θ_t^* and h/z_{max}, for water propagating on a hydrophobic surface ($\theta = 120°$) covered with pillars. Here G^*_{min} is the areal Gibbs free energy density for the composite interface. The two minima in the areal Gibbs free energy density at $h/z_{max} \sim 0$ and $h/z_{max} \sim 1$ correspond to a composite and a metastable fully wetted interface respectively. The inset shows a schematic of the solid substrate. **b.** Top view of the energy diagram shown in Fig. S3a. **c.** The change in the areal Gibbs free energy density, as a function of θ_t^* and h/z_{max}, for

hexadecane propagating on an oleophilic ($\theta = 80°$) surface covered with pillars. Here G^*_{min} is the areal Gibbs free energy density for the fully-wetted interface. For this system, we only observe a single minimum in free energy corresponding to the fully-wetted interface. **d.** Top view of the energy diagram shown in Fig. S3c.
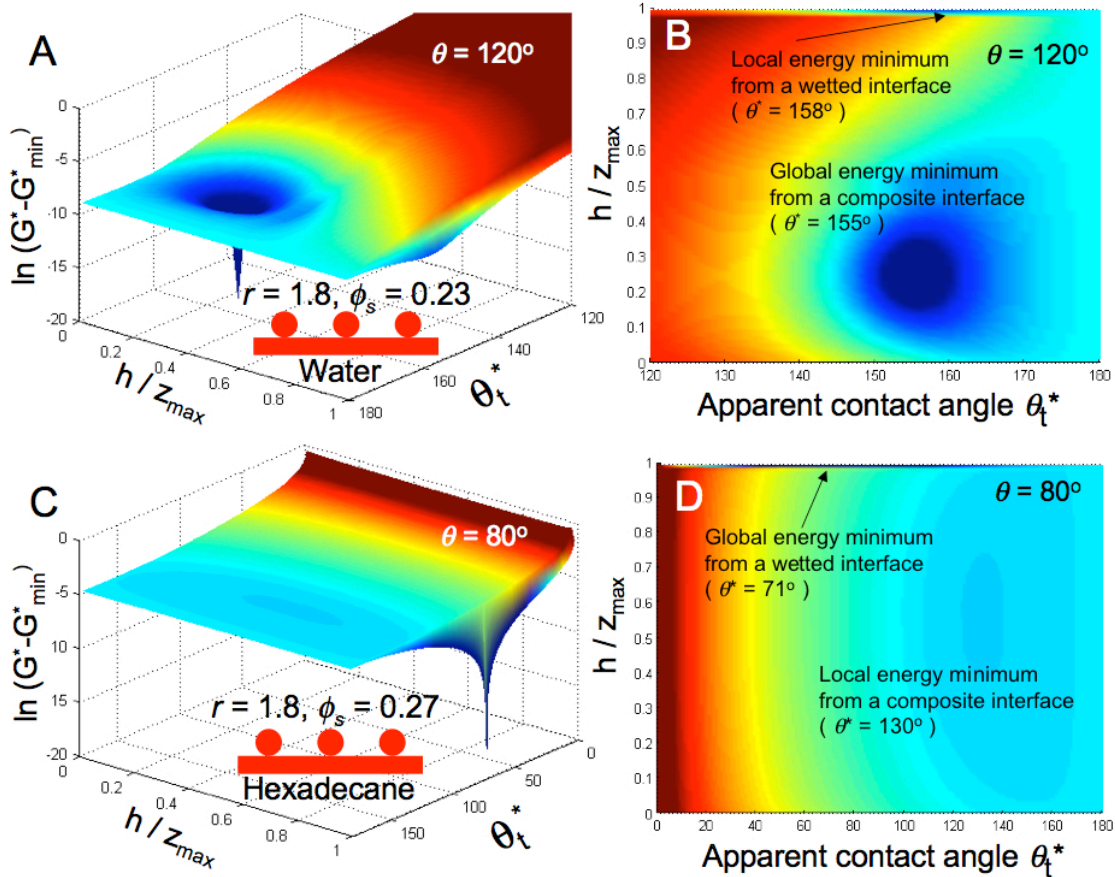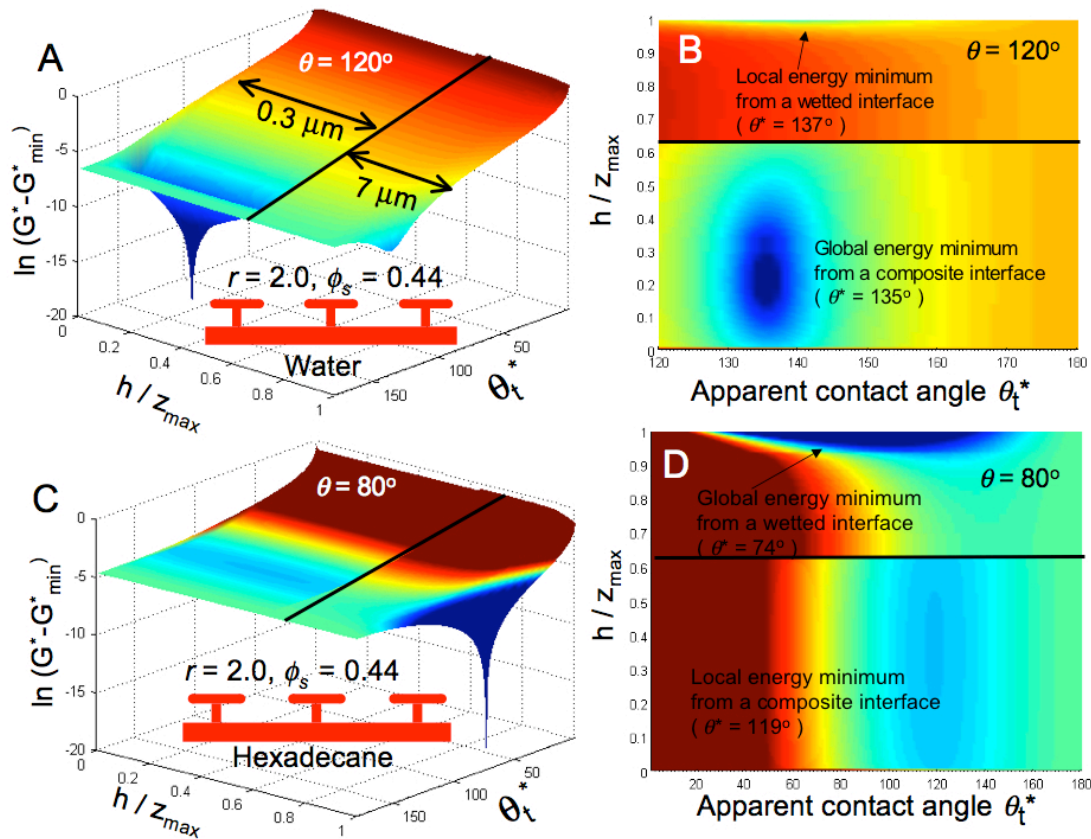

Figure S4a. The change in the areal Gibbs free energy density, as a function of θ_t^* and h/z_{max}, for water propagating on a hydrophobic ($\theta = 120°$) electrospun surface. Here G^*_{min} is the areal Gibbs free energy density for the composite interface. The two minima in the areal Gibbs free energy density at $h/z_{max} \sim 0.25$ and $h/z_{max} \sim 1$ correspond to a composite and a metastable fully wetted interface respectively. The inset shows a schematic of the solid substrate. **b.** Top view of the energy diagram shown in Fig. S4a. **c.** The change in the areal Gibbs free energy density, as a function of θ_t^* and h/z_{max}, for hexadecane propagating on an oleophilic ($\theta = 80°$) electrospun surface. Here G^*_{min} is the areal Gibbs free energy density for the fully-wetted interface. In contrast to the surface covered with vertical pillars, for the electrospun surface we observe a metastable composite interface corresponding to a local minimum in free energy at $h/z_{max} \sim 0.6$. **d.** Top view of the energy diagram shown in Fig. S4c.

Figure S5a. The change in the areal Gibbs free energy density, as a function of θ_t^* and h/z_{max}, for water propagating on a hydrophobic ($\theta = 120°$) micro-hoodoo surface. Here G^*_{min} is the areal Gibbs free energy density for the composite interface. The two minima in the areal Gibbs free energy density at $h/z_{max} \sim 0.025$ and $h/z_{max} \sim 1$ correspond to a composite and a metastable fully wetted interface respectively. The inset shows a schematic of the solid substrate. For all parts of Fig. S5, the *y*-axis (h/z_{max}) is spaced unequally, based on the thickness of the hoodoo caps ($2R = 0.3$ µm) and height of the hoodoos ($H = 7$ µm), for easier visualization of the minimum in free energy corresponding to the composite interface. This leads to the discontinuity, highlighted with the added straight line, visible in each figure. **b.** Top view of the energy diagram shown in Fig. S5a. **c**. The change in the areal Gibbs free energy density, as a function of θ_t^* and h/z_{max}, for hexadecane propagating on an oleophilic ($\theta = 80°$) micro-hoodoo surface. Here G^*_{min} is the areal Gibbs free energy density for the fully-wetted interface. For hexadecane propagating on the micro-hoodoo surface we again observe a metastable composite interface corresponding to a local minimum in free energy at $h/z_{max} \sim 0.05$. **d.** Top view of the energy diagram shown in Fig. S5c.

Section 3. Computation of the breakthrough pressure using Gibbs free energy analysis.
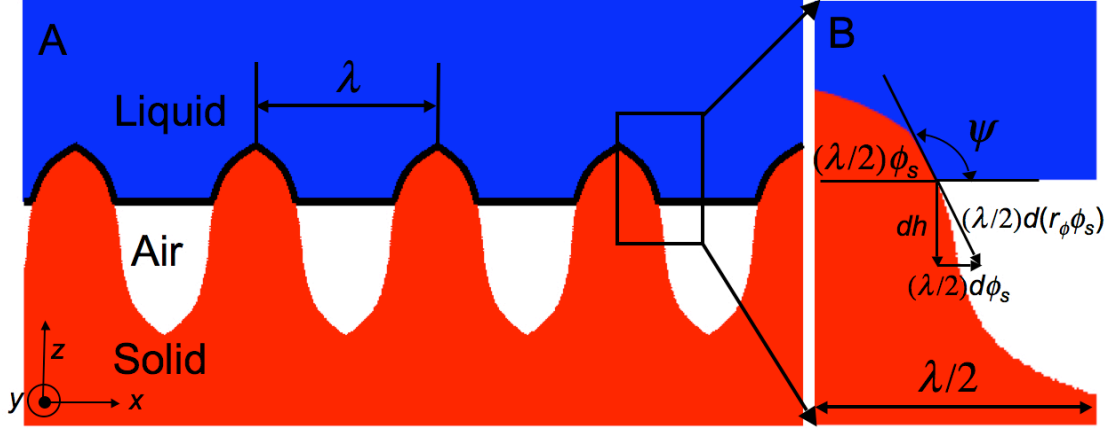
Figure S6. A schematic illustrating the formation of a composite interface and highlighting the various texture parameters used in the calculation of the breakthrough pressure, described below. The local liquid-vapor interface is assumed to be approximately flat as $2D << \ell_{cap}$.

A composite interface formed by a liquid on any solid texture is thermodynamically stable if it corresponds to a minimum in the overall free energy for the system, as explained in detail in supporting information section 1. The surface texture also affects the robustness of a composite interface, and we can use analysis of Gibbs free energy to compute the breakthrough pressure i.e. the external pressure required to force the composite interface to transition irreversibly to the fully wetted interface.

If we assume the internal pressure within a liquid volume pushes at the composite interface, the work done on the composite interface by the pressure (W_p) should be equal to the change in interfacial energy of the composite interface (E_{comp}), i.e.

$$\delta W_p = dE_{comp} \qquad \text{(s3-1)}$$

When the composite interface moves by the amount equal to dz, the amount of energy per unit area stored in the composite interface $E_{comp}/Area$ is changed by

$$d\gamma_{comp} = d\left(E_{comp} / Area\right) = d\left(r_\phi \phi_s \left(\gamma_{sl} - \gamma_{sv}\right) - \phi_s \gamma_{lv}\right)$$

Now, using Young's relation (12) $\cos\theta = (\gamma_{sv} - \gamma_{sl}) / \gamma_{lv}$,

9

$$d\gamma_{comp} = -d\left(r_\phi \phi_s \cos\theta + \phi_s\right)\gamma_{lv} \qquad \text{(s3-2)}$$

This change in the areal free energy density should be equal to the energy input from the pressure, which can be defined as $\delta\left(W_p / Area\right) = P\delta V / Area = P\left(1-\phi_s\right)dh$ (see Fig. S6), where $\left(1-\phi_s\right)$ is the fraction of the liquid-vapor interface (only the liquid-vapor interface is distorted on the application of external pressure). Thus, the external pressure required to force the composite interface to penetrate into the surface texture by an additional depth 'dh', from a position where the liquid-vapor interface makes an angle ψ with the local geometry (Fig. S6b), can be computed as:

$$P = \frac{-d\left(r_\phi \phi_s \cos\theta + \phi_s\right)\gamma_{lv}}{\left(1-\phi_s\right)dh} = \frac{-\gamma_{lv}}{\left(1-\phi_s\right)}\frac{d\left(r_\phi \phi_s \cos\theta + \phi_s\right)}{dh} = \frac{-\gamma_{lv}}{\left(1-\phi_s\right)}\left(\frac{d\left(r_\phi \phi_s\right)}{d\phi_s}\frac{d\phi_s}{dh}\cos\theta + \frac{d\phi_s}{dh}\right)$$

From Fig. S6b, it is clear that $\sin\left(\psi - \dfrac{\pi}{2}\right) = \dfrac{d\phi_s}{dr_\phi \phi_s}$ or $\dfrac{d\left(r_\phi \phi_s\right)}{d\phi_s} = -\dfrac{1}{\cos\psi}$ and

$\tan\left(\psi - \dfrac{\pi}{2}\right) = \dfrac{(\lambda/2)d\phi_s}{dh}$ or $\dfrac{(\lambda/2)d\phi_s}{dh} = -\dfrac{1}{\tan\psi}$. Therefore,

$$P = \frac{-\gamma_{lv}}{\left(1-\phi_s\right)}\left(\frac{-\cos\theta}{\cos\psi}+1\right)\frac{d\phi_s}{dh} = \frac{-\gamma_{lv}}{\left(1-\phi_s\right)}\left(\frac{-\cos\theta}{\cos\psi}+1\right)\frac{-2}{\lambda\tan\psi} = \frac{2\gamma_{lv}\left(\cos\psi - \cos\theta\right)}{\left(1-\phi_s\right)\lambda\sin\psi} \quad \text{(s3-3)}$$

Here λ is the inter-feature distance or the pitch, as shown in Fig. S6. Eq. s3-3 shows that the pressure required to force the liquid-vapor interface to penetrate into the solid texture increases rapidly as $\psi \to 0°$. Further, once the liquid-vapor interface reaches the bottom of a structure possessing re-entrant curvature, such as an electrospun or a micro-hoodoo surface (for both these surfaces $\psi_{min} = 0°$), so that $\psi = 0°$, Eq. s3-3 predicts that an infinite amount of pressure is required to further propagate the liquid-vapor interface, leading to the formation of a fully wetted interface. These predictions are in stark contrast to our experimental measurements of finite breakthrough pressures for various liquids on both the electrospun and micro-hoodoo surfaces. The errors in the breakthrough pressure predictions from Eq. s3-3 are a direct consequence of the assumption of a flat liquid-vapor interface. In actual experiments, on the application of external pressure,

10

considerable local sagging and distortion of the liquid-vapor interface can occur and the actual failure of the composite regime typically originates from the sagging of the liquid-vapor interface, as explained in detail in the main manuscript.

Section 4. The robustness parameters H^*, T^* and the robustness factor A^*
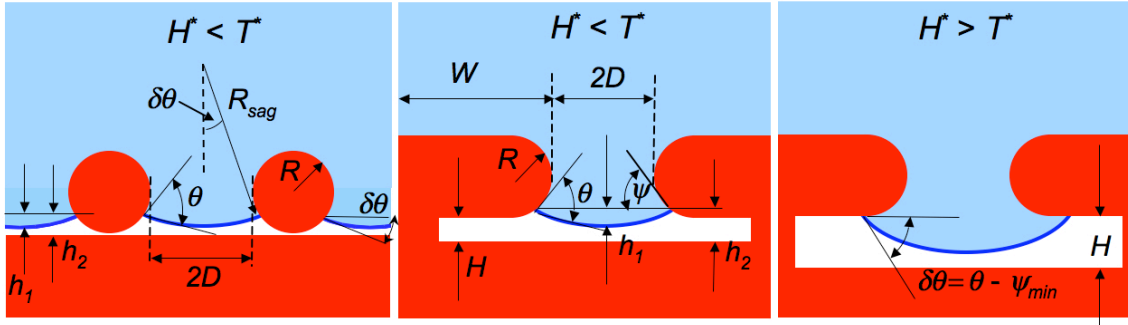
Figure S7. A cartoon highlighting the pressure-induced distortion of the liquid-vapor interface, on the electrospun fiber surfaces and the micro-hoodoos. The geometric parameters R, D, H and W for the various surfaces are also shown. R_{sag} is the radius of curvature of the sagging composite interface. While the composite interfaces shown in Fig. S7a and S7b transition to a fully-wetted interface when the liquid-vapor interface touches the bottom of the relatively shallow pore, the transition for the composite interface in Fig. S7c to a fully-wetted interface happens when the distorted liquid-vapor interface reaches the end of the re-entrant surface texture (or when $\delta\theta = \theta - \psi_{min}$).

Derivation of the robustness height (H^*):

For the electrospun surfaces, the transition from the composite interface to the fully-wetted interface, that occurs on the application of external pressure, is due to the impingement of the sagging liquid-air interface into the next layer of fibers. Thus, the first robustness parameter H^* compares the pressure (P_H) required to force the sagging height (h_1) for the liquid-vapor interface to reach the maximum pore depth h_2 (see Fig. S7a), with the reference pressure $P_{ref} = 2\gamma_{lv} / \ell_{cap}$. The reason for scaling P_H with respect to the reference pressure is that P_{ref} is close to the minimum pressure difference across the composite solid-liquid-air interface for millimetric sized droplets on an omniphobic, textured surface (see supporting information – Section 5 for more details).

Our derivations for both the robustness parameters, T^* and H^*, are based on the

11

generalized force balance, between the pressure inside the liquid (P) and the surface tension (γ_{lv}), which may be written as:

$$P \cdot (interfacial\ area) = \gamma_{lv} \cdot (contact\ line\ length) \cdot \sin \delta\theta \qquad \text{(s4-1)}$$

From Fig. S7a, it can be seen that when the sagging interface reaches the bottom of the pore, the pore depth (h_2) for the electrospun surfaces can be given as:

$$h_2 = R(1 - \cos\theta) \qquad \text{(s4-2)}$$

Further, for the electrospun fiber geometry the variables R_{sag} (the radius of curvature of the sagging composite interface), θ, $\delta\theta_{fiber}$ (sagging angle for the fiber geometry) and h_2 (Fig. S7a) can be correlated as:

$$h_2 = R_{sag}\left(1 - \cos\delta\theta_{fiber}\right) \approx \frac{1}{2}R_{sag}\sin^2\delta\theta_{fiber} \qquad \text{(this approximation holds true for}$$

small values of $\delta\theta$.

Thus we can re-write, $h_2 = \dfrac{1}{2}R_{sag}\left(\dfrac{D}{R_{sag}}\right)^2 = \dfrac{1}{2}\dfrac{D^2}{R_{sag}} \qquad \text{(s4-3)}$

Thus from Eqs. s4-2 and s4-3,

$$R(1 - \cos\theta) \approx \frac{D^2}{2R_{sag}} \rightarrow R_{sag} \approx \frac{D^2}{2R(1 - \cos\theta)} \qquad \text{(s4-4)}$$

If L_{fiber} is the length of an electrospun fiber, we can re-write the force balance (Eq. s4-1) for the system as:

$$P_H \cdot 2D \cdot L_{fiber} = \gamma_{lv} \cdot 2 \cdot L_{fiber} \cdot \sin\delta\theta_{fiber}$$

$$\text{or } 2P_H \cdot D = 2\gamma_{lv}\sin\delta\theta_{fiber} \qquad \text{(s4-5)}$$

Thus, from Eqs. s4-2, s4-4 and s4-5, we can determine P_H as:

$$P_H = \frac{\gamma_{lv}\sin\delta\theta_{fiber}}{D} = \frac{\gamma_{lv}}{R_{sag}} \approx \frac{2\gamma_{lv}R(1 - \cos\theta)}{D^2} = \frac{2h_2\gamma_{lv}}{D^2} \qquad \text{(s4-6)}$$

Thus, the robustness height H^* for the electrospun fiber surfaces becomes:

$$H^* = \frac{P_H}{P_{ref}} = \frac{2\gamma_{lv}R(1 - \cos\theta)\big/D^2}{2\gamma_{lv}\big/\ell_{cap}} = \frac{R\ell_{cap}(1 - \cos\theta)}{D^2} \qquad \text{(s4-7)}$$

Next, we start our analysis for the micro-hoodoo geometry by first considering infinitely

long, stripe-shaped micro-hoodoos for simplicity (referred to as '1D' or striped hoodoos) and expand it for actual synthesized micro-hoodoo structures (discrete micro-hoodoos), similar to the structures shown in Fig. S8b and S8c, later in this section.

For the striped micro-hoodoo surface, schematically shown in Fig. S7b, the pore depth h_2 becomes $R(1-\cos\theta)+H$, instead of $R(1-\cos\theta)$. Further, as was seen before (Eq. s4-3), the variables R_{sag}, θ, $\delta\theta_{striped}$ (sagging angle for the striped hoodoo geometry) and h_2 are correlated by the following geometrical relationship:

$$h_2 = R_{sag}\left(1-\cos\delta\theta_{striped}\right) \approx \frac{1}{2}\frac{D^2}{R_{sag}}$$

Therefore, as before,

$$P_H = \frac{\gamma_{lv}\sin\delta\theta_{striped}}{D} = \frac{\gamma_{lv}}{R_{sag}} \approx \frac{2\gamma_{lv}R\left(\left(1-\cos\theta\right)+H\right)}{D^2} \tag{s4-8}$$

which results in the following expression for the striped micro-hoodoo surface:

$$H^* = \frac{P_H}{P_{ref}} = \frac{R\ell_{cap}\left(\left(1-\cos\theta\right)+H\right)}{D^2} \tag{s4-9}$$

Derivation of the robustness angle (T^*):

We start by deriving the robustness angle T^* for the striped micro-hoodoo geometry. For a striped micro-hoodoo geometry with a large pore depth, as shown in Fig. S7c, the composite (solid-liquid-vapor) interface transitions to the fully-wetted interface when $\delta\theta = \theta - \psi_{min}$, as described in the main manuscript. Thus, we may re-write the overall force balance (s4-1) as:

$$2\gamma_{lv}\sin\delta\theta_{striped} = 2\gamma_{lv}\sin\left(\theta-\psi_{min}\right) = 2D\cdot P_\theta \tag{s4-10}$$

where P_θ is the pressure required to force a sagging angle of $\delta\theta = \theta - \psi_{min}$, as discussed in the main manuscript. Thus, Eq. s4-10 may be re-written as:
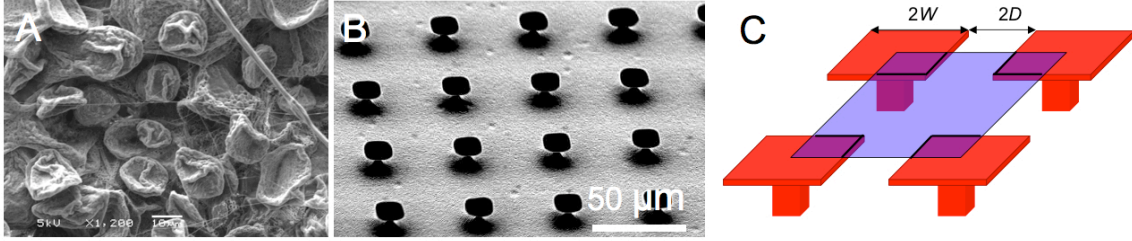
$$P_\theta = \frac{\gamma_{lv}\sin\left(\theta-\psi_{min}\right)}{D} \tag{s4-11}$$

Therefore, we can define the robustness angle T^* as:

$$T^* = \frac{P_\theta}{P_{ref}} = \frac{\dfrac{\gamma_{lv}\sin\left(\theta - \psi_{min}\right)}{D}}{\dfrac{2\gamma_{lv}}{\ell_{cap}}} = \frac{\ell_{cap}\sin\left(\theta - \psi_{min}\right)}{2D} \qquad (s4\text{-}12)$$

T^* for electrospun fiber surfaces is the same as Eq. s4-12, because T^* is independent of the micro-hoodoo height H.

Derivation of H^* and T^* for discrete micro - hoodoos.

Figure S8a. and b. SEM micrographs of the beads-only and the discrete micro-hoodoo surface respectively. **c.** A schematic illustration of the discrete micro-hoodoo geometry.

For structures such as electrospun beads-only surface (Fig. S8a) or discrete micro-hoodoo surface (Figs. S8b and S8c), the robustness parameters H^* and T^* take a different form in comparison to the one-dimensional striped hoodoo surfaces discussed earlier. To derive these parameters, we again start with the generalized force balance (Eq. s4-1), which for the discrete micro-hoodoo structure shown in Figs. S8b and S8c, becomes:

$$P_H \cdot \left(\left(W + D\right)^2 - W^2\right) = 2W\gamma_{lv}\sin\delta\theta_{discrete} \qquad (s4\text{-}13)$$

By comparing Eq. s4-8 and Eq. s4-13, we get

$$\sin\delta\theta_{discrete} = \sin\delta\theta_{striped}\left(\frac{2WD + W^2}{2WD}\right) = \sin\delta\theta_{striped}\left(\frac{1 + \dfrac{W+D}{D}}{2}\right) = \sin\delta\theta_{striped}\left(\frac{1 + \sqrt{D^*}}{2}\right) \quad (s4\text{-}14)$$

Because $D^* \geq 1$, the sagging angle for the discrete hoodoo geometry ($\delta\theta_{discrete}$) is always greater than the corresponding sagging angle for the striped hoodoo structures ($\delta\theta_{striped}$). Further, the difference between $\delta\theta_{discrete}$ and $\delta\theta_{striped}$ becomes larger with increasing values of D^* (or as ϕ_s decreases). Based on Eqs. s4-9 and s4-14, H^* and T^* for the discrete

hoodoos or the electrospun beads-only surfaces (for these structures $H = 0$), can be easily defined as:

$$H^* = \frac{2\ell_{cap}\left(R(1-\cos\theta)+H\right)}{D^2\left(1+\sqrt{D^*}\right)} \ , \ T^* = \frac{\ell_{cap}\sin\left(\theta-\psi_{min}\right)}{D\left(1+\sqrt{D^*}\right)} \tag{s4-15}$$

The definitions of the three design parameters (D^*, T^* and H^*) for the various surfaces synthesized in this work are summarized in Table S1.

Table S1. The three design parameters (D^*, H^* and T^*) for the various surfaces synthesized in this work. The design parameters for the electrospun surfaces with the beads-on-strings morphology are the same as the design parameters for the electrospun surfaces with the fibers-only morphology.

	D^*	H^*	T^*
Electrospun Fibers	$(R+D)/R$	$\left(\dfrac{R\ell_{cap}}{D^2}\right)(1-\cos\theta)$	$\left(\dfrac{\ell_{cap}}{2D}\right)\sin\left(\theta-\psi_{min}\right)$
Electrospun Beads	$(R+D)/R$	$\dfrac{2R\ell_{cap}}{\left[D^2\left(1+\sqrt{D^*}\right)\right]}(1-\cos\theta)$	$\left(\dfrac{\ell_{cap}}{D}\right)\left[\dfrac{\sin(\theta-\psi_{min})}{1+\sqrt{D^*}}\right]$
Discrete Micro-Hoodoos	$((W+D)/W)^2$	$\dfrac{2R\ell_{cap}}{\left[D^2(1+\sqrt{D^*})\right]}\left[(1-\cos\theta)+\dfrac{H}{R}\right]$	$\left(\dfrac{\ell_{cap}}{D}\right)\left[\dfrac{\sin(\theta-\psi_{min})}{1+\sqrt{D^*}}\right]$

Derivation of the combined robustness factor A^*.
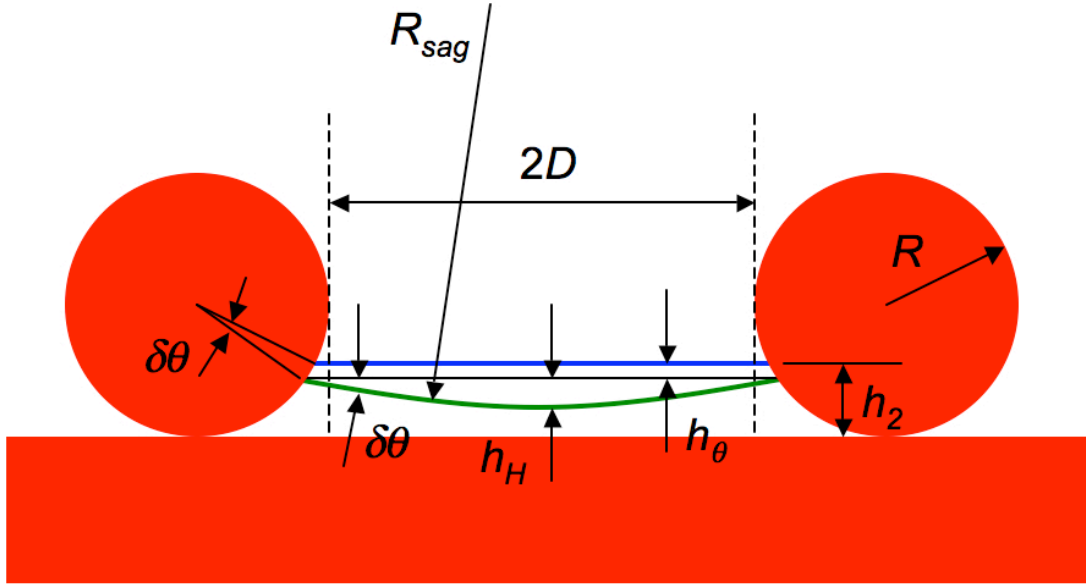
Figure S9. Detailed schematic diagram of the liquid-vapor interface distortion due to external pressure. On the application of external pressure, the original liquid-air interface (shown in blue) sags downward to new position (shown in green) by the amount equal to h_H, but the contact line between the interface and the solid moves downward as well by h_θ.

Robustness parameters H^* and T^* are derived based on the assumption that the sagging height (h_1) and the sagging angle ($\delta\theta$) are independent of each other. However, on the application of external pressure on a liquid-vapor interface, both h_1 and $\delta\theta$ increase simultaneously, and therefore the real robustness for the composite interface can be much lower than the prediction by either H^* or T^* individually. As an example, consider Fig. S9, which shows the deformation of the liquid-vapor interface on the electrospun fiber mats. If the droplet's internal pressure is equal to the reference pressure $P_{ref} = 2\gamma_{lv} / \ell_{cap}$, the radius of curvature (κ) of the distorted liquid-vapor interface is given as $\kappa = R_{sag}^{-1}$ ($= 2\ell_{cap}^{-1}$ for our reference drop). The total sagging height (h_{total}) is the sum of the two heights h_H and h_θ (as shown in Fig. S9), which can be both computed as:

$$h_H = R_{sag}\left(1 - \cos\delta\theta_{fibers}\right) \approx R_{sag}\sin^2\delta\theta_{fibers} = \frac{D^2}{2R_{sag}} = \frac{D^2}{\ell_{cap}}$$

16

as the robustness height $H^* = \dfrac{(1-\cos\theta)R\ell_{cap}}{D^2}$, therefore $h_H = \dfrac{R(1-\cos\theta)}{H^*}$ (s4-16)

Further,

$$h_\theta = R\left(\cos(\theta-\delta\theta)-\cos\theta\right) = R\left(2\sin\left(\frac{2\theta-\delta\theta}{2}\right)\sin\frac{\delta\theta}{2}\right) \approx 2R\sin\theta\sin\frac{\delta\theta}{2}$$

$$\approx R\sin\theta\sin\delta\theta = \frac{RD\sin\theta}{R_{sag}} = \frac{2RD\sin\theta}{\ell_{cap}}$$

as $T^* = \dfrac{\ell_{cap}\sin(\theta-\psi_{min})}{2D}$, therefore $h_\theta = \dfrac{R\sin^2\theta}{T^*}$ (s4-17)

Thus, from Eqs. s4-16 and s4-17, the total sagging height (h_{total}) can be calculated as:

$$h_{total} = h_H + h_\theta = \frac{R(1-\cos\theta)}{H^*} + \frac{R\sin^2\theta}{T^*}$$ (s4-18)

Again, from Fig. S7a, it can be seen that when the sagging interface reaches the bottom of the pore, the pore depth (h_2) for the electrospun surfaces can be given as:

$$h_2 = R(1-\cos\theta)$$ (s4-19)

Next, if we define A^* as the ratio between the pressure needed to reach the next fiber layer scaled with the reference pressure, then by analogy to our derivation of the robustness height H^* (also see Eq. s4-6), the combined robustness factor A^* becomes:

$$A^* = \frac{P_{breakthrough}}{P_{ref}} = \frac{R(1-\cos\theta)}{\dfrac{R(1-\cos\theta)}{H^*}+\dfrac{R\sin^2\theta}{T^*}} = \frac{1}{\dfrac{1}{H^*}+\dfrac{\sin^2\theta}{(1-\cos\theta)T^*}}$$

or $\dfrac{1}{A^*} = \dfrac{1}{H^*} + \dfrac{\sin^2\theta}{(1-\cos\theta)T^*}$ (s4-20)

which is a particular form of a harmonic mean between H^* and T^*. In general the robustness factor (A^*) may be written as:

$$\frac{1}{A^*} = \frac{C_1}{H^*} + \frac{C_2}{T^*}$$ (s4-21)

where the coefficients C_1 and C_2 are a function of the exact surface geometry. For our surfaces, based on Eq. s4-20, and recognizing that $\dfrac{\sin^2\theta}{(1-\cos\theta)} \sim O(1)$ (this approximation

works well for all values of $\theta < 90°$, provided $\theta \neq 0°$), we approximate the coefficients as $C_1 \approx C_2 \approx 1$, to yield:

$$\frac{1}{A^*} \approx \frac{1}{H^*} + \frac{1}{T^*}$$

(s4-22)

Our computed values of A^* for all synthesized micro-hoodoo surfaces are provided in Table S2. This table also provides the measured breakthrough pressures with octane, as well as the values of the other corresponding design parameters – D^*, T^* and H^*.

Table S2. The surface characteristics for the various silanized micro-hoodoo surfaces synthesized, the computed values for the various design parameters and the advancing and receding contact angles with octane (γ_{lv} = 21.7 mN/m, θ = 55°), as well as the corresponding breakthrough pressures with octane, arranged in ascending order of the measured breakthrough pressure.

Sample	θ^*_{adv}	θ^*_{rec}	W (μm)	H (μm)	D (μm)	D^*	H^*	T^*	A^*	Measured breakthrough pressure (Pa)
1	162°	144°	10	3	20	9	6.8	18	4.9	61.2
2	161°	143°	10	4	20	9	9	18	6.0	80
3	162°	141°	10	3	15	6.3	14	28	9.2	91.2
4	163°	143°	10	7	20	9	16	18	8.5	113
5	162°	142°	10	4	15	6.3	18	28	11	244
6	161°	141°	10	7	15	6.3	32	28	15	175
7	158°	142°	10	3	10	4	36	49	21	232
8	160°	141°	10	7	10	4	84	49	31	863
9	159°	132°	10	3	5	2.3	173	118	70	>1400
10	159°	134°	10	7	5	2.3	403	118	91	>1400

Section 5. The significance of the reference pressure P_{ref}.
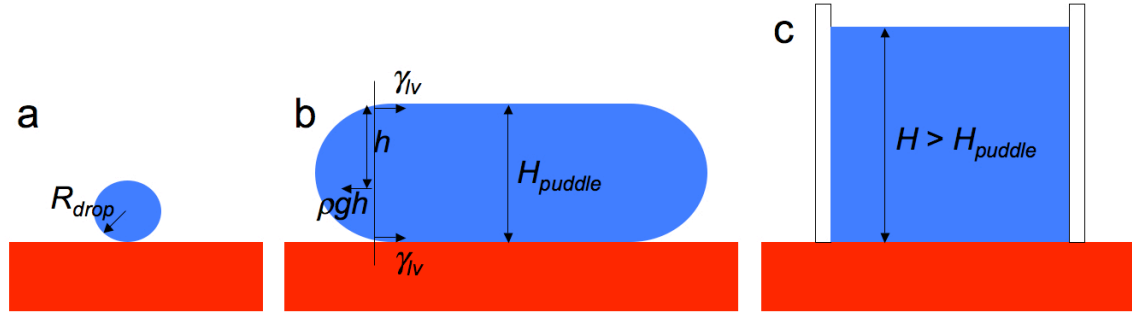
Figure S10. A schematic illustrating the various shapes of a liquid volume on an omniphobic surface. (a) A liquid droplet adopts the shape of perfect sphere when $R_{drop} \ll \ell_{cap}$ or $Bo \ll 1$. (b) A liquid volume forms a puddle when $Bo \gg 1$. (c) A schematic of a large volume of liquid confined within a tube.

When a liquid contacts a hypothetical omniphobic surface (assuming $\theta^* \sim 180°$), the liquid volume reaches an equilibrium shape that is determined by a balance between gravity and the surface tension of the liquid. When the size of the liquid volume is much smaller than the capillary length ($\ell_{cap} = \sqrt{\gamma_{lv}/\rho g}$), i.e. Bond number, $Bo \ll 1$ where $Bo = \rho g R_{drop}^2 / \gamma_{lv}$ (here ρ is the liquid density, g is the acceleration due to gravity, R_{drop} is the droplet radius which scales with the liquid volume $V^{1/3}$ and γ_{lv} is the liquid surface tension), the shape of the droplet approaches a perfect sphere as shown in Fig. S10a. As more liquid is added to the droplet, the droplet surface starts to flatten due to gravity, and when the bond number $Bo \gg 1$, the liquid shape looks similar to the shape of a puddle, as shown in Fig. S10b. In such a case, the pressure at the bottom of the puddle can be simply computed as:

$$P_{puddle} = \rho g H_{puddle} \tag{s5-1}$$

where H_{puddle} is the height of the liquid puddle as shown in Fig. S10b. A horizontal force balance, equating the forces resulting from the surface tension and the pressure inside the liquid volume, can be used to determine the puddle height H_{puddle}, as shown below:

$$2\gamma_{lv} = \int_{0}^{H_{puddle}} \rho g h \, dh = \frac{1}{2}\rho g \left(H_{puddle}\right)^2$$

$$\rightarrow H_{puddle} = \sqrt{\frac{4\gamma_{lv}}{\rho g}} = 2\ell_{cap} \tag{S5-2}$$

Thus, the pressure at the bottom of the puddle is given as:

$$P_{puddle} = \rho g H_{puddle} = 2\sqrt{\gamma_{lv}\rho g} = \frac{2\gamma_{lv}}{\ell_{cap}} = P_{ref} \tag{S5-3}$$

For a liquid column with a height $H > H_{puddle}$ in a confined area as shown in Fig. S10c, it is obvious that the pressure at the bottom of the column will always be greater than P_{ref}. On the other hand, the pressure difference across the composite interface for liquid droplets with diameter $2R_{drop} \ll H_{puddle}$ is governed by Laplace pressure ($P_{Laplace} = 2\gamma_{lv}/R_{drop}$), which also leads to much higher pressure than P_{ref} if $R_{drop} < \ell_{cap}$. As we compute the breakthrough pressure for a composite interface using the relation $P_{breakthrough} = A^* \times P_{ref}$, it is clear that when the robustness factor $A^* = 1$, $P_{breakthrough} = P_{ref}$. Since P_{ref} is close to the minimum pressure across the composite interface for any liquid volume with $\theta^* = 180°$, any surface for which $A^* < 1$, will be unable to support a composite interface with a given contacting liquid. It is possible to select other reference pressures to scale the breakthrough pressure; for example for a membrane of perfectly non-wetting circular close-packed pores of diameter 2D, $P_{ref-pores} = 2\gamma_{lv}/D$. However,

using $P_{ref} = 2\gamma_{lv} / \ell_{cap}$ as the scaling pressure ensures that the threshold value for the crossover between the composite and fully-wetted interface is $A^* \approx 1$.

Section 6. Re-entrant textures with $\psi_{min} < 0^o$

For a given liquid, the robustness angle (T^*) for a composite interface is directly proportional to sin ($\theta - \psi_{min}$). This implies that as long as ($\theta - \psi_{min}$) < 90°, lower values of the geometry angle ψ_{min} enable higher values of T^* or the formation of a more robust composite interface. In this work, we have developed two different families of structures, for both of which $\psi_{min} = 0°$. It is also possible to imagine hypothetical geometries for which $\psi_{min} < 0°$ as shown below:
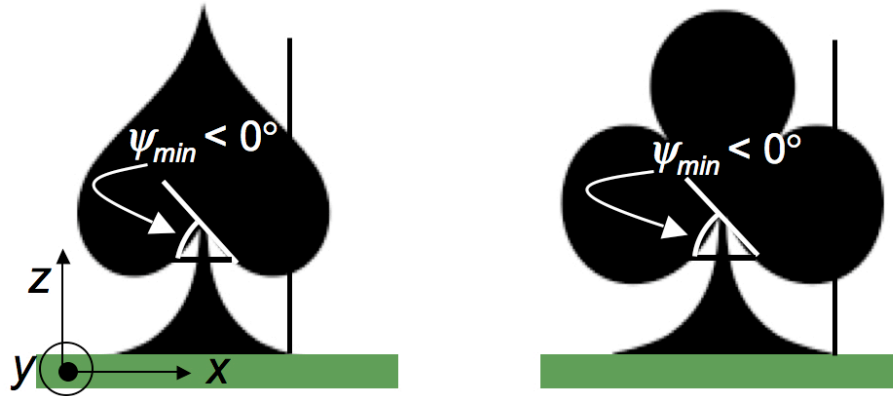
Figure S11. Two proposed surface textures possessing re-entrant curvature with ψ_{min} <0°. It can also be seen that a vector projected normal to the *x-y* plane intersects this re-entrant geometry more than once.

Section 7. Dip-coating a lotus leaf.

Low surface tension liquids such as rapeseed oil (γ_{lv} = 35.7 mN/m) easily wet the surface of many naturally superhydrophobic surfaces, such as duck feathers and the lotus leaf. However, once the lotus leaf is dip-coated in a solution of fluorodecyl POSS (see methods), it is able to support a composite interface and high apparent contact angles with rapeseed oil, as shown in Fig. S12.

Figure S12. Droplets of rapeseed oil (γ_{lv} = 35.7 mN/m, η = 70 mPa.s, θ = 86°, θ^* = 141°) on a lotus leaf dip-coated in a solution of fluorodecyl POSS.

**Section 8:** Surface energy of various PMMA + fluorodecyl POSS blends.

There are several different methods of using contact angles to estimate the surface energy (γ_{sv}) of a material; for example the Zisman analysis (13), the Owens-Wendt analysis (14), and Girifalco-Good-Fowkes-Young (15, 16) analysis. However, each of these methods typically yields a different value for the computed surface energy, depending on the surface under study (17). The problem stems from the fact that the measurement of equilibrium contact angles only provides an indirect estimate of the surface energy, as the various methods for surface energy computation typically involve extrapolation or assume an additive decomposition of γ_{sv} into dispersive and H-bonding / polar contributions. The most accurate determination of surface energies requires the measurement of the work of adhesion, and this is not often done (17). Thus, previous studies have noted that these methods should only be used to obtain an estimate of the actual surface energy, which can be useful in comparing and ranking different surfaces (say with different degree of fluorination) provided the same experimental method is used for each surface (17).

Based on the above understanding, we have computed the surface energy of our PMMA + fluoroPOSS surfaces using both the Zisman and the Owens-Wendt methods. The samples for both these analysis were prepared by spin-coating smooth, thin films (18) of various PMMA + fluoroPOSS blends, on a silicon wafer. The Owens-Wendt analysis was performed by using water (with a dispersive component of surface tension, $\gamma_{lv}^{d} = 21.1$ mN/m, and polar component $\gamma_{lv}^{p} = 51.0$ mN/m) and octane ($\gamma_{lv}^{d} = 21.7$ mN/m and $\gamma_{lv}^{p} = 0.0$ mN/m) as the polar and dispersive liquids respectively. Thus, using the Owens-Wendt analysis, we can compute the dispersive (γ_{sv}^{d}) and polar (γ_{sv}^{p}) components of the solid surface energy as:

$$2\begin{bmatrix} \sqrt{\gamma_{water}^{d}} & \sqrt{\gamma_{water}^{p}} \\ \sqrt{\gamma_{octane}^{d}} & \sqrt{\gamma_{octane}^{p}} \end{bmatrix}\begin{bmatrix} \sqrt{\gamma_{sv}^{d}} \\ \sqrt{\gamma_{sv}^{p}} \end{bmatrix} = \begin{bmatrix} (1+\cos(\theta_{water}))\gamma_{water} \\ (1+\cos(\theta_{octane}))\gamma_{octane} \end{bmatrix} \qquad \text{(s7-1)}$$

For a spincoated surface containing 44.4 wt% POSS we obtain values of $\gamma_c = -3$ mN/m and $\gamma_{sv} = 11.1$ mN/m ($\gamma_{sv}^{d} = 11.0$ mN/m, $\gamma_{sv}^{p} = 0.1$ mN/m) using the Zisman and

the Owens-Wendt methods respectively. Here γ_c is the critical surface tension defined as the minimum value for the surface tension of a liquid that will fully wet a given solid substrate. The critical surface tension γ_c is taken as an indirect estimate of the solid surface energy γ_{sv}. Fig. S13(a) shows the Zisman analysis for four different spincoated PMMA + fluoroPOSS films, while Fig. S13(b) shows the results from the Owens-Wendt analysis.
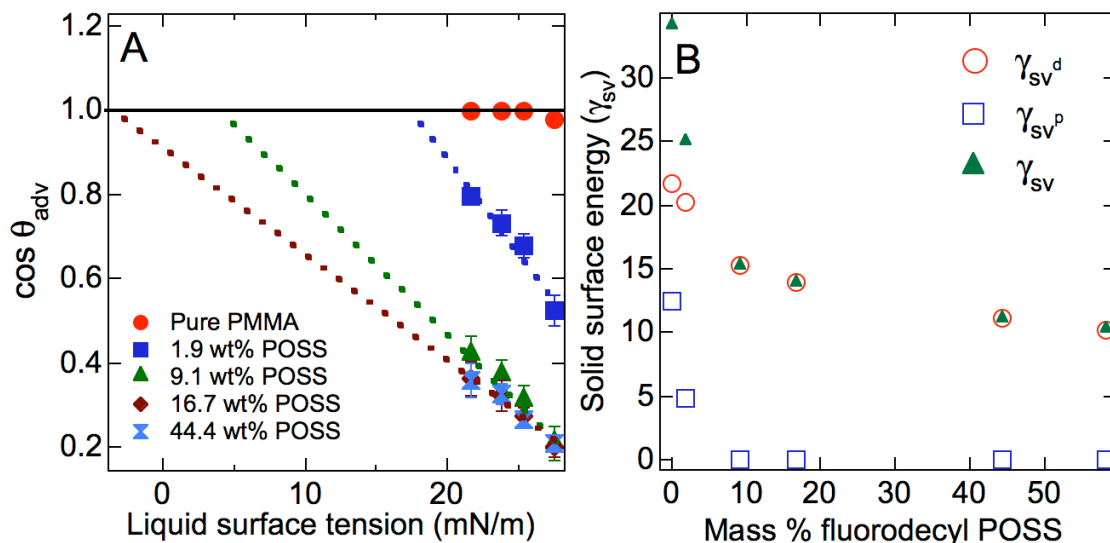
Figure S13a. Zisman plot for various spincoated PMMA + fluorodecyl POSS films. The analysis was performed by measuring the advancing contact angles against a homologous series of alkanes, octane (γ_{lv} = 21.7 mN/m), decane (γ_{lv} = 23.8 mN/m), dodecane (γ_{lv} = 25.3 mN/m) and hexadecane (γ_{lv} = 27.5 mN/m). The critical values of surface tension obtained from the extrapolation are γ_c(1.9 wt%) = 18.7 mN/m; γ_c(9.1 wt%) = 6.6 mN/m; γ_c(16.7 wt%) = -2.2 mN/m; γ_c(44.4 wt%) = -3 mN/m. **b.** Results from Owens-Wendt analysis for various spincoated PMMA + fluorodecyl POSS films. The analysis was performed by using water and octane as the polar and dispersive liquids respectively.

Clearly, the negative value of the surface energy obtained from the Zisman analysis of our surfaces are spurious and arise solely from the linear extrapolation process employed in the process. However, these calculations again point out the limitations of the various methods that use measurements of equilibrium contact angles to compute γ_{sv}. It is however clear from the data in Fig. S13 that, as would be expected, the surface energy of our PMMA + fluoroPOSS blends decreases with increasing POSS concentration.

References.

1. Wenzel RN (1936) Resistance of solid surfaces to wetting by water. Ind. & Eng. Chem. 28, 988–994.
2. Cassie ABD & Baxter S (1944) Wettability of porous surfaces. Trans. Faraday Soc. 40, 546–551.
3. Marmur A (2003) Wetting on Hydrophobic Rough Surfaces: To Be Heterogeneous or Not To Be? Langmuir 19, 8343-8348.
4. He B, Patankar NA, & Lee J (2003) Multiple Equilibrium Droplet Shapes and Design Criterion for Rough Hydrophobic Surfaces. Langmuir 19, 4999-5003.
5. Lafuma A & Quéré D (2003) Superhydrophobic states. Nature Mater. 2, 457-460.
6. Nosonovsky M & Bhushan B (2008) Patterned Nonadhesive Surfaces: Superhydrophobicity and Wetting Regime Transitions. Langmuir 24, 1525-1533.
7. Extrand CW (2002) Model for contact angles and hysteresis on rough and ultraphobic surfaces. Langmuir 18, 7991-7999.
8. Oner D & McCarthy T (2000) Ultrahydrophobic Surfaces. Effects of Topography Length Scales on Wettability. Langmuir 16, 7777-7782.
9. Barbieri L, Wagner E, & Hoffmann P (2007) Water Wetting Transition Parameters of Perfluorinated Substrates with Periodically Distributed Flat-Top Microscale Obstacles. Langmuir 23, 1723-1734.
10. Callies M, Chen Y, Marty F, Pépin A, & Quéré D (2005) Microfabricated textured surfaces for super-hydrophobicity investigations. Microelectronic Engineering 78-79, 100-105.
11. Gao L & McCarthy TJ (2006) The "Lotus Effect" Explained: Two Reasons Why Two Length Scales of Topography Are Important. Langmuir 22, 2966-2967.
12. Young T (1805) An Essay on the Cohesion of Fluids. Philos. Trans. R. Soc. London 95, 65.
13. Zisman WA (1964) Relation of the equilibrium contact angle to liquid and solid construction. In Contact Angle, Wettability and Adhesion, ACS Advances in Chemistry Series. (American Chemical Society, Washington, DC.).
14. Owens DK & Wendt RC (1969) Estimation of the surface free energy of polymers. J. Appl. Poly. Sci. 13, 1741-1747.
15. Girifalco LA & Good RJ (1957) A Theory for the Estimation of Surface and Interfacial Energies. I. Derivation and Application to Interfacial Tension. J. Phys. Chem. 61, 904-909.
16. Fowkes FM (1964) Attractive Forces at Interfaces. Ind. Eng. Chem. 56, 40-52.
17. Owen MJ & Kobayashi H (1994) Surface active fluorosilicone polymers. Macromol. Symp. 82, 115-123.
18. Tuteja A, Choi W, Ma ML, Mabry JM, Mazzella SA, Rutledge GC, McKinley GH, & Cohen RE (2007) Designing superoleophobic surfaces. Science 318, 1618-1622.
19. Richard D & Quéré D (2000) Bouncing water drops. Europhys. Lett., 769.